

Radiative effect of aerosols above the northern and southern Atlantic Ocean as determined from shipborne lidar observations

T. Kanitz,¹ A. Ansmann,¹ P. Seifert,¹ R. Engelmann,¹ J. Kalisch,¹ and D. Althausen¹

Received 28 February 2013; revised 31 October 2013; accepted 1 November 2013; published 26 November 2013.

[1] The direct solar radiative effect of aerosols over the Atlantic Ocean was investigated on the basis of aerosol Raman/polarization lidar observations aboard the research vessel *Polarstern* between Germany (50°N) and either South America (50°S) or South Africa (40°S) in 2009 and 2010. First, a case study of complex aerosol conditions with marine aerosol, dust, and smoke particles in the boundary layer and free troposphere is presented to demonstrate that detailed knowledge of aerosol layering (boundary layer, free troposphere) and aerosol mixing state is required for an accurate determination of the resulting radiative effects. A statistical analysis based on all lidar observations revealed the highest daily mean radiative effect ($-43 \pm 59 \text{ W m}^{-2}$ at the surface, $-14 \pm 18 \text{ W m}^{-2}$ at top of atmosphere) in the latitudinal belt from 0°N–15°N in the Saharan dust outflow region. Mean aerosol radiative effects of the polluted northern and clean southern midlatitudes were contrasted. In the northern midlatitudes, the averaged aerosol radiative effect of all simulations was $-24 \pm 33 \text{ W m}^{-2}$ at the surface which is a factor of 1.6 higher than at similar southern hemispheric latitudes. The simulations based on the lidar observations are in good agreement with colocated pyranometer measurements.

Citation: Kanitz, T., A. Ansmann, P. Seifert, R. Engelmann, J. Kalisch, and D. Althausen (2013), Radiative effect of aerosols above the northern and southern Atlantic Ocean as determined from shipborne lidar observations, *J. Geophys. Res. Atmos.*, 118, 12,556–12,565, doi:10.1002/2013JD019750.

1. Introduction

[2] The Earth's energy budget is a result of complex interactions of a multitude of processes in the atmosphere [Trenberth *et al.*, 2009]. One reason for the high uncertainties in current climate prediction modeling [Forster *et al.*, 2007] is the spatial and temporal variability of aerosols [Textor *et al.*, 2006] as well as the variations in the aerosol microphysical properties as size, shape, and chemical composition. Global aerosol models embedded in chemistry-transport or general circulation models have begun to resolve the aerosol vertical distribution and have validated their results with height-resolved observations [e. g., Koffi *et al.*, 2012]. However, in radiative transfer models, aerosols are often approximated simply by an unrealistic exponential increase in the aerosol load from the top of atmosphere (TOA) to the surface [Shettle, 1979; Haywood and Shine, 1997; Mayer and Kylling, 2005].

[3] The need for height-resolved measurements was shown by Wendisch *et al.* [1996] who studied combined airborne in situ and radiation measurements under atmospheric conditions with two temperature inversions that sensitively influenced the vertical distribution of aerosols. Keil and Haywood [2003] determined a conversion from the usual cooling effect of aerosols to a warming effect at TOA by biomass-burning aerosol during cloud-free and cloudy observations during the Southern African Aerosol Regional Science Initiative (SAFARI 2000).

[4] In addition to airborne in situ observations of aerosols, lidars are suitable to obtain the vertical distribution of lofted aerosol layers, cloud base heights, or profiles of the extinction coefficient to perform radiative transfer calculations [Redemann *et al.*, 2000; Podgorny and Ramanathan, 2001; Johnson *et al.*, 2008; Mallet *et al.*, 2008; Bauer *et al.*, 2011].

[5] To our knowledge, Wagner *et al.* [2001] presented the first radiative transfer calculations that directly included height-resolved aerosol information as determined with lidar [Ansmann *et al.*, 2000] during the Indian Ocean Experiment. Single scattering albedo and asymmetry parameter were inverted using optical properties derived from multiwavelength lidar measurements [Müller *et al.*, 1999]. Profiles of the extinction coefficient and its spectral dependence as determined with lidar in the framework of the European Aerosol Research Lidar Network [Mattis *et al.*, 2004] were used to investigate the feasibility of simple backscatter lidars to determine the solar aerosol radiative effect and to improve in this way the estimation of aerosol effects on Earth's radiation budget [Wendisch *et al.*, 2006]. However, a validation

¹Leibniz Institute for Tropospheric Research, Leipzig, Germany.

Corresponding author: T. Kanitz, Leibniz Institute for Tropospheric Research, Permoserstr. 15, DE-04318 Leipzig, Germany. (kanitz@tropos.de)

©2013. The Authors. *Journal of Geophysical Research: Atmospheres* published by Wiley on behalf of the American Geophysical Union. This is an open access article under the terms of the Creative Commons Attribution-NonCommercial-NoDerivs License, which permits use and distribution in any medium, provided the original work is properly cited, the use is non-commercial and no modifications or adaptations are made. 2169-897X/13/10.1002/2013JD019750

of the findings with colocated radiation measurements was missing both times.

[6] Huang *et al.* [2009] used extinction profiles of a dust plume from the Taklimakan desert as determined from spaceborne lidar observations by the Cloud-Aerosol Lidar with Orthogonal Polarization (CALIOP) [Winker *et al.*, 2009] in radiative transfer calculations to determine the aerosol effect more realistically. Single scattering albedo, asymmetry parameter, and spectral dependencies were adjusted to colocated radiation measurements of the cloud and the Earth's energy budget scanner [Wielicki *et al.*, 1996].

[7] In the presented paper the vertical distribution of aerosols above the Atlantic as determined with a shipborne Raman/polarization lidar between 51°N and 53°S [Kanitz *et al.*, 2013] was used to perform one-dimensional plane-parallel radiative transfer calculations and to contrast the direct aerosol effect on the solar radiation budget in the Northern and Southern Hemispheres over the Atlantic based on observed profiles of aerosol properties. In section 2, the applied instruments will be presented. Afterward, a case study of an aerosol layer of a mixture of Saharan dust and biomass-burning smoke will show the necessity of Raman/polarization lidar measurements to derive accurate aerosol profile information for radiative transfer calculations. Section 4 presents a north-south cross section of the direct aerosol effect on the solar radiation budget over the Atlantic and the results from an intensive comparison to shipborne pyranometer observations. Concluding remarks are given in section 5.

2. Experiment

[8] In the framework of the OCEANET project, the transfer of energy and material between ocean and atmosphere was investigated aboard the German research vessel *Polarstern* during three meridional cruises [Macke *et al.*, 2010]. Continuous observations of aerosol and cloud profiles with lidar, temperature and humidity profiles, and liquid-water path with microwave radiometer, incident solar and thermal radiation with pyranometer and pyrgeometer, as well as sensible and latent heat fluxes with turbulence and CO₂ flux measurements were performed to determine the radiative budget at the surface of the highly variable atmosphere [e.g., Kalisch and Macke, 2012]. Vertical aerosol profiling was performed with lidar to determine the latitudinal cross section of the direct solar aerosol radiative effect. The transfer routes between the Northern and Southern Hemispheres offered an excellent opportunity to contrast aerosol conditions and underlying processes between both hemispheres [Kanitz *et al.*, 2011; 2013]. The first cruise went from Bremerhaven, Germany (16 October 2009, ANT-XXVI/1) to Punta Arenas, Chile (25 November 2009). Here, the lidar was unmounted from the ship and deployed at the University of Magallanes, Punta Arenas for a 4 month measurement campaign (4 December 2009 to 4 April 2010). Afterward, the lidar was remounted at the ship to go from Punta Arenas (7 April 2010, ANT-XXVI/4) back to Bremerhaven (17 May 2010). The last cruise started in Bremerhaven (25 October 2010, ANT-XXVII/1) toward Cape Town, South Africa (25 November 2010), which was concluded by a 4 month lidar measurement campaign

in Stellenbosch, South Africa from 2 December 2010 to 13 April 2011 [Kanitz *et al.*, 2013].

2.1. OCEANET-Atmosphere

[9] In the framework of OCEANET, particle extinction profiles were determined from measurements of the multiwavelength Raman/polarization lidar Polly^{XT} [Althausen *et al.*, 2009] at 355 and 532 nm by measuring the nitrogen vibrational Raman signals at 387 and 607 nm [Ansmann *et al.*, 1990]. Profiles of the extinction-related Ångström exponent [Ångström, 1929] were determined from the extinction values at 355 nm and 532 nm wavelength [Ansmann *et al.*, 2002] for radiative transfer calculations, too. Particle backscatter coefficients at 355, 532, and 1064 nm were determined with the Raman method [Ansmann *et al.*, 1992]. Thus, aerosol layers were characterized in terms of the extinction-to-backscatter ratio and Ångström exponents [Müller *et al.*, 2007]. During daytime and high solar background, particle extinction and backscatter coefficient profiles were determined with the Klett method considering the lidar ratio as derived during nighttime and stable atmospheric conditions [Klett, 1981; Sasano *et al.*, 1985]. In addition, the 355-nm particle linear depolarization ratio was determined as described by Freudenthaler *et al.* [2009] to discriminate spherical and nonspherical aerosol particles [Tesche *et al.*, 2009].

[10] In the near range at heights below about 350–400 m, the incomplete overlap between the transmitted laser beams and the receiver field of view prohibits the measurement of reliable lidar return signals (minimum height). Below this height, the backscatter and extinction values in the marine boundary layer (MBL) were set constant and equal to values determined for 400 m height. So, we assume a well-mixed MBL at heights <400 m on the basis of our gained experience during the analysis of the entire shipborne lidar data set [Kanitz *et al.*, 2013]. In addition, the profile of the extinction coefficient between 400 and 1000 m was corrected with an overlap function as explained in Wandinger and Ansmann [2002].

[11] Radiation measurements were performed in the solar range from 305 to 2800 nm with the pyranometer Kipp and Zonen CM21 following the ISO9060 standard with a resolution of 1 s and an uncertainty of $\pm 2\%$ [Kipp and Zonen, 2004]. Including effects of the ship movements and the ship's superstructure, e.g., the crew's nest, we assume an uncertainty of $\pm 4\%$.

[12] A sky imager [Kalisch and Macke, 2008] took four pictures of the hemisphere above OCEANET-Atmosphere each minute at daytime. The pictures yield the information about cloud coverage.

2.2. Library Radiative Transfer (libRadtran)

[13] The UVSPEC program [Kylling, 1992] of the libRadtran library version 1.6-beta was chosen to calculate the broadband solar downward and upward irradiances at the surface to derive the direct solar aerosol radiative effect [Mayer and Kylling, 2005]. The libRadtran library includes the discrete ordinate solver DISORT version 2.0 [Stamnes *et al.*, 1988] and the spectral integration by the correlated-k approximation [Kato *et al.*, 1999]. DISORT was applied with 16 streams with respect to the built-in bidirectional reflectance distribution function (BRDF) [Cox and Munk,

1954a, 1954b; *Bellouin et al.*, 2004] for the surface albedo. The dependence of the surface albedo on the 10 m surface wind speed and thus on the sea swell was considered based on the wind speed measurements of RV *Polarstern* (1 min resolution) whenever data were available. Solar zenith angles were determined as a function of ship position and time [*Blanco-Muriel et al.*, 2001]. Particle-free and cloud-free atmospheric conditions were described with standard atmospheres [*Anderson et al.*, 1986] as implemented in libRadtran for trace gases and with profiles of pressure, temperature, and relative humidity from the Global Data Assimilation System 1 [*Kanamitsu*, 1989]. The profiles of the meteorological standard parameters are provided with $1^\circ \times 1^\circ$ resolution every 3 h. Vertically resolved aerosol conditions were included in terms of the lidar-derived extinction profiles. Single scattering albedo and asymmetry parameter were taken from the literature in dependence of the lidar-derived aerosol type [*Dubovik et al.*, 2002; *Fiebig and Ogren*, 2006; *Müller et al.*, 2011; *Heinold et al.*, 2011]. The vertical model grid was set to the maximum resolution of 0.1 km below 6 km height and to 1 km above. The lidar-derived extinction profiles were downscaled to that grid. The comparisons to pyranometer measurements were performed in the spectral range from 305 to 2800 nm in agreement to the detected range of the pyranometer.

3. Observations and Calculations

[14] On the basis of the lidar observations during three meridional cruises of *Polarstern*, one-dimensional radiative transfer calculations were performed and compared to colocated pyranometer measurements. In the following, we will present our approach in detail for a case of complex dust/smoke layering. Afterward, we show an overall comparison to the pyranometer measurements, which motivated a statistical analysis of the north-south cross section of the direct solar aerosol radiative effect over the Atlantic Ocean.

3.1. Case Study—Mixed Dust/Smoke Layer

[15] During the second *Polarstern* cruise ANT-XXVI/4, extended lofted aerosol layers were observed off the west coast of northern Africa from 8°N – 21°N , 23°W (over 1400 km) between 30 April 2010 and 5 May 2010. Figure 1 shows the lidar measurements from 18:00 UTC on 30 April to 8:00 UTC on 2 May 2010 together with simultaneous pyranometer measurements. Short-time minima in the pyranometer measurements and white coloring in the lidar height-time display (strong backscatter) indicate the frequent occurrence of MBL clouds on 1 May. In the lidar measurements, two lofted aerosol layers were first detected at 19:00 UTC on 30 April 2010 (Figure 1). The lower layer extended roughly from 1.3 to 1.9 km height, the upper layer from 2.4 to 3.5 km height. With lidar, we derived aerosol optical thicknesses (AOTs) of the free-tropospheric aerosol of about 0.2 from the extinction profiles at 532 nm (Figure 2, left). Mean extinction-related Ångström exponents were 0.8. The particle linear depolarization ratio was, on average, $21\% \pm 2\%$ in the upper layer and $22\% \pm 3\%$ in the lower layer which indicates the presence of nonspherical dust particles. Nevertheless, the layer mean Ångström exponent was higher than the typical value for pure dust (of around 0), and the 355 nm particle linear depolarization ratio was smaller

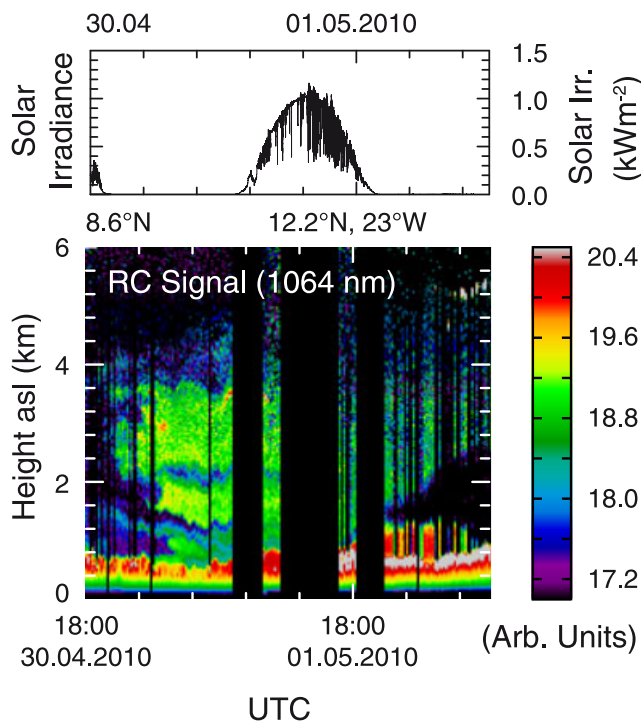


Figure 1. (top) Solar irradiance measured with pyranometer and (bottom) height-time display of the range-corrected 1064-nm lidar backscatter signal from 18:00 UTC on 30 April to 8:00 UTC on 2 May 2010, showing complex aerosol layering of dust and smoke above 800 m height and the marine boundary layer below. Lidar overlap effects (for heights <400 m) are not corrected. Black columns in the height-time display result from measurement interruptions due to high solar altitude and maintenance.

than the pure dust values of $>26\%$ [*Freudenthaler et al.*, 2009; *Groß et al.*, 2011b]. Mean lidar ratios of 59–61 sr at 355 nm were in the range of pure dust-related lidar ratios of 48–70 sr and mixed-dust related lidar ratios of 57–98 sr [*Groß et al.*, 2011b]. These values indicate a mixture of dust and biomass-burning smoke aerosol in agreement with findings from the Saharan Mineral Dust Experiment at Cape Verde (SAMUM-2) [*Tesche et al.*, 2011]. After *Tesche et al.* [2009], the fractions of dust and smoke can be derived on the basis of the particle linear depolarization ratio. In this study, we assumed a particle linear depolarization ratio of 25%–29% for pure dust and of 3%–5% for smoke [*Kanitz et al.*, 2013]. By means of this approach, a smoke fraction of roughly 30% was determined.

[16] On the basis of the lidar-derived extinction profiles, the direct solar aerosol radiative effect was determined. Single scattering albedo (SSA) and asymmetry parameter for dust, smoke, and marine aerosol were adapted from *Dubovik et al.* [2002] as presented in Table 1. The authors found typically higher asymmetry parameters with Sun photometer for smoke than reported from in situ measurements before [*Reid et al.*, 1998]. Taking into account that the asymmetry parameter for smoke derived from lidar observations during SAMUM-2 was lower as well [*Tesche et al.*, 2011], we decided to decrease the asymmetry parameter generally by 10%.

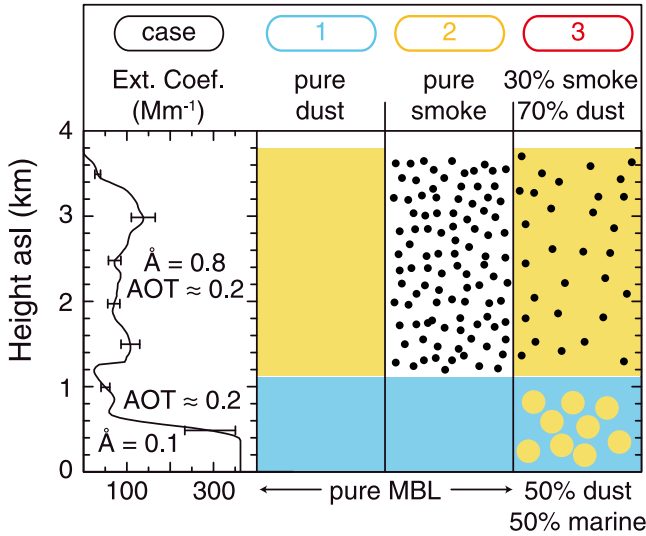


Figure 2. Overview of aerosol conditions assumed in the radiative transfer calculations for 1 May 2010. The microphysical properties are listed in Table 1.

[17] An overview of the aerosol conditions used in the following calculations is given in Figure 2. Three different scenarios were assumed in the radiative transfer simulations. Calculations were performed for lofted layers of pure dust or pure smoke in the presence of a pure marine MBL (cases 1 and 2). In addition, for case 3, the mixing ratio of smoke and dust in the free troposphere was set to 30%:70% as derived with lidar. Furthermore, a mixed MBL with a dust and marine particle fraction of each 50% was assumed, reflecting the observed comparably high AOT of the MBL and the significantly enhanced depolarization at the top of the MBL [Groß *et al.*, 2011a; Kanitz *et al.*, 2013]. The surface albedo was estimated for a mean wind speed of 5.5 m s^{-1} in the simulations.

[18] Figure 3b shows the observed irradiance (black line) at the surface on 1 May 2010 from 6:00 to 18:00 UTC. Simplified calculations for nonmixed aerosol layers (cases 1 and 2, blue and orange lines) are presented, too. In between is the modeled irradiance that includes a MBL with a fraction of 50% dust and a lofted layer with a smoke fraction of 30% (case 3, red line) as suggested from the lidar analysis. Overall, the simulations show a promising agreement with the diurnal process of the pyranometer measurements, despite the peaks in the measurement due to unconsidered clouds. However, the uncertainties in the radiative transfer calculations remain high because of the atmospheric variability during the day as well as the uncertainty of assumed input parameters. Especially, the necessary assumption of the microphysical parameters is crucial [Tegen and Lacis, 1996; Liao and Seinfeld, 1998; Sokolik *et al.*, 2001]. In the case of smoke, the single scattering albedo can range between 0.6 and 0.93 in dependence of the combustion process, the fuel type, and the aging process as discussed in Dubovik *et al.* [2002] and Reid *et al.* [2005]. For smoldering and aged smoke, only small deviations were found and single scattering albedos approaching roughly 0.93. Dust-related microphysical properties are influenced by the chemical composition, the size distribution, and the

nonspherical shape of the dust particles [Tegen and Lacis, 1996; Mishchenko *et al.*, 1997; Sokolik and Toon, 1999; Otto *et al.*, 2009; Osborne *et al.*, 2011]. However, Dubovik *et al.* [2002] presented a comprehensive data set of microphysical properties of different aerosol types and source regions on the basis of AERONET Sun photometer observations which were adapted in our calculations. For an overall error analysis, we varied the main input parameters as shown in Table 2. The largest uncertainty is produced from the assumed single scattering albedo.

[19] In addition, the extinction profile changed according to the evolution of the dust plume during the day (Figure 1). Changes in the profiles of temperature and relative humidity were considered in our calculations only with low time resolution of 3 h. Depolarization and three-dimensional effects caused by inhomogeneities of the aerosol layers were not considered in the simulation. For example, peaks in the observed downward irradiance above the modeled irradiance for cloud-free conditions (Figure 3b) are the result of three-dimensional effects by the broken-cloud field [Schade *et al.*, 2007]. However, under consideration of Table 2, counterbalancing effects [Roger *et al.*, 2006], and the generally good agreement between the pyranometer measurements and the modeling results (Figure 3b), we assume an uncertainty of roughly 15% at the surface and 20% at the TOA.

[20] Figure 3a shows the results of the performed simulations and the pyranometer measurements in more detail. The modeled irradiance for an aerosol-free atmosphere (green) is highest. The simulation of a mixed lofted layer that includes 30% smoke (red, case 3) agrees well with the measured incident irradiance. In the case of a pure dust layer, the modeled irradiance is slightly higher than the measured irradiance (case 1, underestimated absorption), whereas it is too low when only a pure smoke layer is considered (case 2, overestimated absorption). Especially the adjusted SSA for the lidar-derived aerosol layer composition is responsible for this agreement. The higher absorption efficiency of smoke [Bond and Bergstrom, 2006] is indicated in Figure 3c by the highest direct solar aerosol radiative effect in the case of pure smoke in the lofted layer (case 2, orange) which reaches up to -102 W m^{-2} (instantaneous) at a solar zenith angle of 40° . The daily mean solar aerosol radiative effect for aerosol conditions determined with lidar (50% dust in the MBL, 30% smoke in the lofted layer) is $-33 \pm 5 \text{ W m}^{-2}$ at the surface and reaches instantaneous values of -78 W m^{-2} . In contrast, the daily mean solar aerosol radiative effect for a pure dust or smoke layer is -26 ± 4 and $-44 \pm 7 \text{ W m}^{-2}$, respectively.

[21] Figure 4 presents the calculation results for TOA. The lowest upward irradiance was obtained for aerosol-free

Table 1. Overview of Single Scattering Albedo (SSA) and Asymmetry Parameter (g) That Were Used in Radiative Transfer Calculations of Dust, Smoke, and Marine Aerosol Observations (Adapted From Dubovik *et al.* [2002])

Wavelength (nm)	Marine SSA/g	Dust SSA/g	Smoke SSA/g
440	0.98/0.75	0.93/0.73	0.79/0.64
670	0.97/0.71	0.98/0.71	0.76/0.53
870	0.97/0.69	0.99/0.71	0.72/0.48
1020	0.97/0.68	0.99/0.71	0.70/0.47

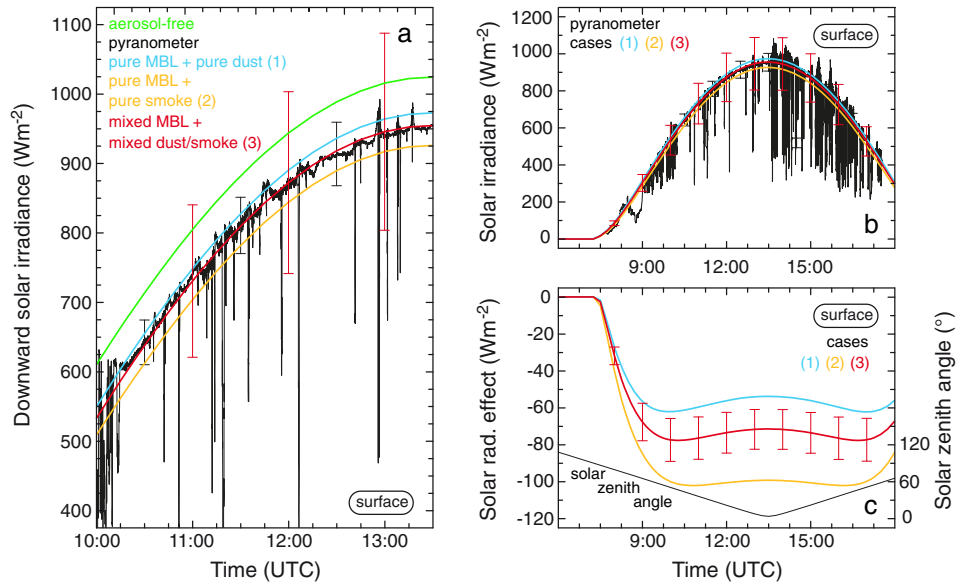


Figure 3. (a) Solar irradiance observed (black) and modeled (colored lines for cases 1, 2, and 3 shown in Figure 2) at the surface on 1 May 2010. (b) Observed (black) and modeled solar irradiance (cases 1, 2, and 3) on 1 May 2010 (6:00 to 18:00 UTC). (c) Direct solar aerosol radiative effect (colored lines indicate the different cases 1, 2, and 3) and solar zenith angle (black). The uncertainty of the simulations is assumed to be 15% and is similar for all curves.

conditions (Figure 4, left, light green). In the presence of aerosol, more incident radiation is scattered to TOA than during aerosol-free conditions over the ocean, i.e., the planetary albedo for incident radiation is increased by the atmospheric albedo in comparison to aerosol-free conditions and an albedo of the ocean water surface of ≈ 0.05 . The simulated upward irradiance at TOA for the aerosol conditions as determined with lidar (red, case 3) are smaller than for the lofted pure dust layer (blue, case 1) and higher than for the lofted pure smoke layer (orange, case 2). The difference reaches instantaneous values of 3.5 and 7.5 W m^{-2} which is a factor of 4–6 smaller than at the surface (Figure 3). The change in the aerosol radiative effect for the different aerosol conditions, i.e., the different microphysical properties (Table 1) is less pronounced at TOA than at the surface (Figure 4, right). The solar radiative effect for aerosol conditions as determined with lidar and supported by the radiative transfer calculations at the surface (red, case 3) reaches values as low as $-39 \pm 8 \text{ W m}^{-2}$. The daily mean radiative effect is $-15 \pm 3 \text{ W m}^{-2}$ which is almost the same for all three scenarios.

[22] In the presented case study daily mean solar radiative efficiencies of -79 W m^{-2} at the surface and of -41 W m^{-2} at TOA were obtained from the radiative transfer calculations under consideration of mixed aerosol layers as suggested from lidar observations. Radiative transfer modeling results of such mixed aerosol layers are rare. During SAMUM-2, *Heinold et al.* [2011] determined mean radiative efficiencies of a mixed dust/smoke plume of -42 W m^{-2} at the surface and $\pm 0 \text{ W m}^{-2}$ at the TOA. The smoke fraction was higher (during the main period of biomass burning in western Africa) than the dust fraction and single scattering albedos were selected for fresh flaming phase smoke. Due to the very low smoke related single scattering albedo, the planetary albedo was almost

the same as for aerosol-free conditions over the ocean surface. Further east close to Niamey, Niger mean radiative efficiencies of mixed dust/smoke plumes of -69.9 W m^{-2} at the surface and -40.0 W m^{-2} at TOA were determined with one-dimensional radiative transfer simulations based on airborne nephelometer measurements of the extinction coefficient in the framework of the Dust And Biomass Experiment (DABEX) [*Johnson et al.*, 2008]. The aircraft measurements were validated with lidar-derived extinction profiles before the calculations.

[23] A promising way to account for the aerosol composition in radiative transfer calculations was presented in the case of mixed aerosol conditions in the free troposphere, resulting in a good agreement to coincident pyranometer measurements. However, the separation of aerosol types in mixed layers is currently a time-consuming approach and inappropriate for the investigation of the role of free-tropospheric aerosol over the Atlantic Ocean during the three meridional trans-Atlantic cruises. In many cases, the free-tropospheric aerosol concentration is very low, the signal-to-noise ratio decreased, and a source apportionment is only possible with additional aerosol transport simulations.

Table 2. Error Budget for Radiative Transfer Simulations of the Solar Aerosol Radiative Effect in Scenario Three Shown in Figure 2 for 1 May 2010

	Δ Solar Aerosol Effect (%)	
	Surface	TOA
$g_{\text{MBL}} \pm 5\%$	± 4	± 6
$g_{\text{FT}} \pm 5\%$	± 3	± 5
$SSA_{\text{MBL}} \pm 5\%$	± 13	± 8
$SSA_{\text{FT}} \pm 5\%$	± 9	± 10
$AOT \pm 10\%$	± 8	± 14
$\text{Wind} \pm 5\%$ (surface albedo)	± 3	± 2

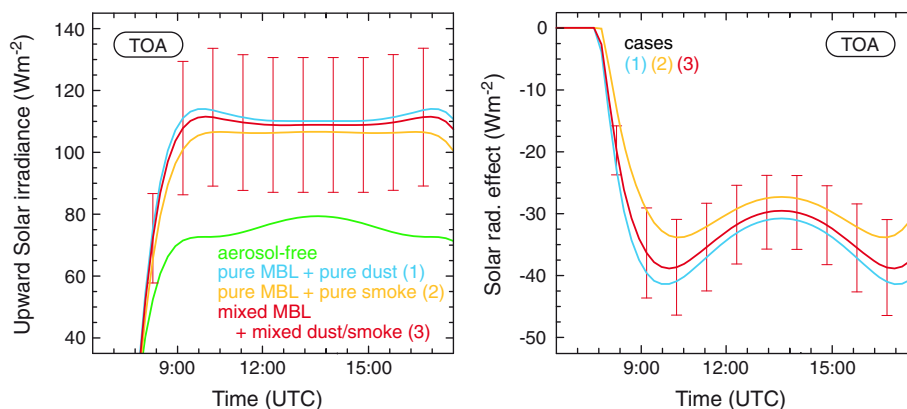


Figure 4. (left) Solar irradiance as modeled (colored lines for cases 1, 2, and 3 shown in Figure 2) at the top of atmosphere (TOA) on 1 May 2010. (right) Respective solar radiative effect at TOA. The uncertainty of the simulations is assumed to be 20% and is similar for all curves.

Thus, in the following section, the aerosol properties used in the radiative transfer calculations are simplified to save computational time at the expense of higher uncertainties.

4. Statistics

[24] Radiative transfer calculations were performed for 246 analyzed lidar measurements. In this effort, the profiles of the aerosol extinction coefficient were approximated by step functions with MBL aerosol (for heights <1000 m, Figure 5, green) and free-tropospheric aerosol (from 1 to 5 km height, Figure 5, red). In the MBL, pure marine aerosol was assumed and treated with an asymmetry parameter of 0.65 and a single scattering albedo of 0.99 [Fiebig and Ogren, 2006; Müller *et al.*, 2011]. In the free troposphere, a rather complex composition of continental aerosols from natural and anthropogenic sources occurs [Mattis *et al.*, 2008] which might be mixed with marine aerosol by entrainment at the MBL top as well. Under these conditions, the single scattering albedo can vary between almost 1 for marine aerosol and sulfate particles, to values >0.8 for dust, urban haze, and smoke from smoldering and to smaller values for fresh smoke from flaming and black carbon [Takemura *et al.*, 2002; Reid *et al.*, 2005; Meloni *et al.*, 2006; Petzold *et al.*, 2011; Kim *et al.*, 2011]. Dubovik *et al.* [2002] presented asymmetry parameters from 0.47 for smoke particles and 0.75 for marine particles in the wavelength range from 440 to 1020 nm. In our simplified approach, we defined a SSA of 0.9 and an asymmetry parameter of 0.62 for the free-tropospheric aerosol which represents a compromise between the main observed and reported free-tropospheric aerosol types over the Atlantic, dust and smoke, respectively [Reid *et al.*, 2004; Tesche *et al.*, 2009; Yu *et al.*, 2010; Duflot *et al.*, 2011; Kanitz *et al.*, 2013; Preißler *et al.*, 2013]. An overview of the idealized aerosol conditions is shown in Figure 5. In addition, the computations were simplified by assuming standard atmospheric conditions [Anderson *et al.*, 1986] and International Geosphere-Biosphere Programme surface-albedo values that are offered in spectral bands for different surface types within libRadtran [Mayer and Kylling, 2005].

[25] The simulation results were then compared with the ground-based pyranometer measurements. Each analyzed

lidar profile was used to determine the downward irradiance at the surface at the position of *Polarstern* during the day (24 h) of the lidar observation in steps of 15 min under the assumption of stable atmospheric conditions. The analyzed lidar data set was cloud screened to ensure that the simulated irradiance was influenced by aerosols only. However, in the observation of irradiance, clouds play an important role. The cloud coverage as determined with the sky imager [Kalisch and Macke, 2008] was considered to classify observations during cloud-free conditions. By default, only these observations can be approximated with the simulations.

[26] Figure 6 shows a scatterplot of the modeled and measured irradiance at the surface for cases with a cloud coverage of less than 30%. In general, the simulations of the irradiance at the surface are in good agreement with the pyranometer measurements. Overestimations of the model result from the presence of small boundary layer clouds exactly in the pathway of the direct incident irradiance which causes a significant additional cloud radiative effect which is not considered in the model [Ramanathan *et al.*, 1989]. Cases with measured irradiance higher than modeled irradiance can occur due to reflections produced by the superstructure

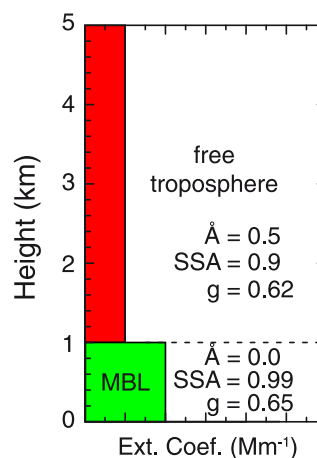


Figure 5. Overview of aerosol profile conditions assumed in radiative transfer calculations for 246 lidar measurements.

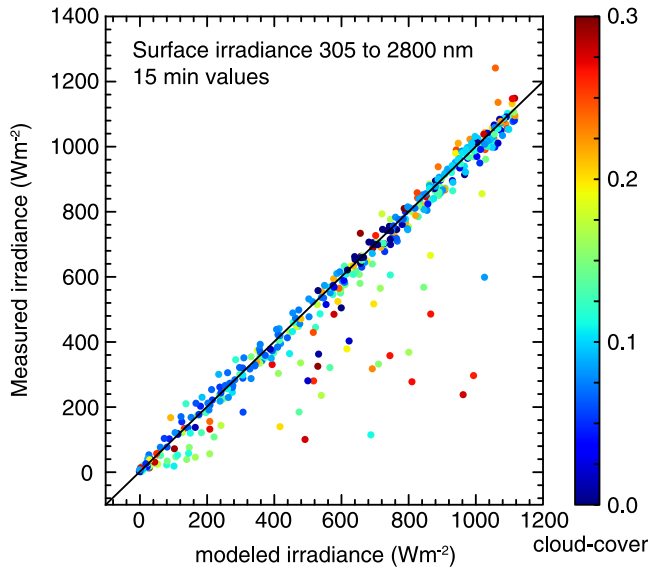


Figure 6. Comparison of modeled and measured solar irradiances at the surface. The color code represents the cloud coverage as determined with a sky imager.

of the ship and scattering by broken clouds at high Sun elevation.

[27] The performed radiative transfer calculations served for the first latitude-dependent investigation of the direct solar aerosol radiative effect based on lidar-derived aerosol profile data. Lidar provides the advantage to discuss the effect of the overall (atmospheric column) aerosol effect under consideration of the contribution of the free tropospheric and boundary-layer aerosol. An overview of the corresponding aerosol conditions is given in terms of the AOT (from 0 to 5 km height) in Table 3. AOTs as derived with hand-held Microtops Sun photometer in the framework of the maritime aerosol network (MAN) from 2004 to 2011 [Smirnov *et al.*, 2009] are shown for comparison. The highest mean AOT (from 0 to 5 km height) was determined in the northern tropics (0°N – 30°N), the outflow region of the Saharan desert. The mean AOT in the southern midlatitudes is roughly half of the mean AOT in the northern midlatitudes. This distinct difference in the aerosol conditions of both midlatitudes is also expressed in terms of the direct solar radiative effect shown in Figure 7 (black circles). At the surface, mean radiative effects of -24 ± 33

Table 3. Overview of the Aerosol Conditions for Certain Latitudinal Belts in Terms of AOT as Determined With Lidar for Different Height Ranges During Three Cruises of *Polarstern* and With Microtops in the Framework of MAN From 2004 to 2011

Latitudinal Belt	AOT 0–5 km	AOT 0–1 km	AOT MAN
60°N – 30°N	0.12 ± 0.06	0.04 ± 0.03	0.13 ± 0.03
30°N – 15°N	0.20 ± 0.09	0.05 ± 0.03	0.2 ± 0.1
15°N – 0°N	0.27 ± 0.14	0.07 ± 0.05	0.27 ± 0.08
0°S – 15°S	0.14 ± 0.07	0.05 ± 0.03	0.12 ± 0.02
15°S – 30°S	0.09 ± 0.05	0.03 ± 0.02	0.09 ± 0.01
30°S – 60°S	0.07 ± 0.05	0.02 ± 0.02	0.07 ± 0.01
Punta Arenas	0.05 ± 0.03	0.02 ± 0.01	
Stellenbosch	0.07 ± 0.03	0.03 ± 0.02	

and $-15 \pm 22 \text{ W m}^{-2}$ were calculated for the northern and the southern midlatitudes (Figure 7, bottom). This difference is caused exclusively by the different aerosol load (AOT), neglecting the complex aerosol composition (SSA, asymmetry parameter) of anthropogenic pollution, desert dust, and biomass-burning smoke in the northern midlatitudes [Mattis *et al.*, 2008]. The number of anthropogenic aerosol sources is much lower in the southern midlatitudes [Dentener *et al.*, 2006]. Aerosol layers in the free troposphere are limited to biomass burning in Australia [Dirksen *et al.*, 2009], South Africa [Duflot *et al.*, 2011], South America [Singh *et al.*, 2000], and dust outbreaks from the Patagonian desert [Kanitz *et al.*, 2013]. The less variable effect of the marine boundary-layer aerosol (0–1 km, Figure 7, green diamonds) possibly suggests a minor role of the boundary-layer aerosol in the determination of the difference between northern and southern midlatitudes. The mean radiative effect is in the range of -3 to -7 W m^{-2} at the surface for all observed latitudinal belts. In the MBL, the permanent aerosol emission of the ocean leads to a uniform aerosol loading (Table 3) with almost nonabsorbing marine aerosol [Müller *et al.*, 2011]. However, the importance of the contribution of marine aerosol to the global aerosol effect is

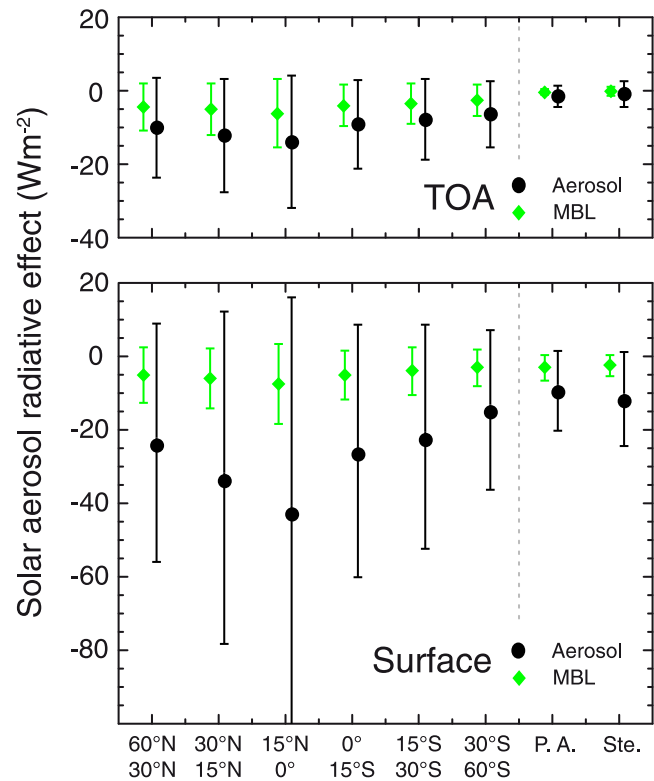


Figure 7. Mean solar aerosol radiative effect at the (top) top of atmosphere (TOA) and the (bottom) surface for different latitudinal belts as determined from libRadtran simulations on the basis of lidar observations performed during three trans-Atlantic cruises of *Polarstern* in 2009 and 2010 as input for the vertical aerosol distribution according to Table 3. Black-filled circles show simulation results including free-tropospheric and boundary-layer aerosol. Green diamonds show results of simulations with only boundary-layer aerosol. Error bars indicate the standard deviation.

due to the global distribution of water surfaces on the Earth [Haywood *et al.*, 1999]. The atmosphere over large remote areas in the Pacific Ocean and the Southern Ocean contains marine aerosol only [Smirnov *et al.*, 2009]. The large error bars in Figure 7 are caused by the variability of the prevailing aerosol conditions and by the different distributions of solar zenith angles at different locations. In addition, the solar radiative effect is a nonmonotonic function of the solar zenith angle with maximum values at intermediate angles [Boucher *et al.*, 1998], which lead to differences of the solar radiative effect of the same aerosol layer in the midlatitudes and tropics.

[28] Within both hemispheres, the direct solar aerosol effect increases in the tropics toward the equator. The highest solar radiative effect occurs in the northern tropics from 15°N to 0°N ($-43 \pm 59 \text{ W m}^{-2}$). Even in the area of the tropics, a step from the northern to the southern hemisphere is visible, which is related to the Saharan dust outflow.

[29] The TOA solar aerosol radiative effect (Figure 7, top) shows the same patterns as a function of latitude as the surface radiative effects (Figure 7, bottom). However, they are smaller in range by a factor of 2–3. In the northern midlatitudes, the solar aerosol radiative effect is $-10 \pm 13 \text{ W m}^{-2}$, in the southern midlatitudes it is $-6 \pm 9 \text{ W m}^{-2}$. Spaceborne instruments found solar aerosol radiative effects of -8 W m^{-2} for the northern midlatitudes above the Atlantic [Kaufman *et al.*, 2005] and -2 W m^{-2} for the latitudinal belt from 20°S to 40°S above the Pacific [Christopher and Zhang, 2002] and confirm the difference between northern and southern midlatitudes. In the northern tropics, direct solar aerosol radiative effects of -13 W m^{-2} (latitudinal belt from 30°N to 10°N) [Christopher and Zhang, 2002] and -14 W m^{-2} (30°N–5°N) [Kaufman *et al.*, 2005] were determined. Based on the lidar measurements of this study, direct solar aerosol radiative effects of -12 ± 16 and $-14 \pm 18 \text{ W m}^{-2}$ were estimated from the simulations for the tropical belts from 30°N to 15°N and from 15°N to 0°N at TOA, i.e., very good agreement to the spaceborne observations is obtained.

[30] The direct solar aerosol radiative effect was also determined for the two measurement campaigns performed in the southern hemisphere. The surface type was changed from ocean surface to grassland (Punta Arenas) and savanna (Stellenbosch). Thus, the absorption efficiency of the surface was reduced. In the boundary layer and the free troposphere, continental aerosol was assumed with the same microphysical properties as in the settings before. At the surface (Figure 7, top), a solar aerosol radiative effect of about -12 and -10 W m^{-2} was determined at Stellenbosch and Punta Arenas, respectively. At Punta Arenas, the lowest determined AOT values [Kanitz *et al.*, 2013] lead also to the lowest determined direct solar aerosol radiative effect. At TOA, the change of the surface albedo from ocean (≈ 0.05) to savanna (≈ 0.18) strongly affects the radiative influence of the aerosol. Although the mean AOT determined at Stellenbosch (0.07) is in the range of the determined AOT for the latitudinal belts from 30°S to 60°S (AOT of 0.08, solar aerosol radiative effect of -6 W m^{-2}) and 15°S–30°S (AOT of 0.08, solar aerosol radiative effect of -8 W m^{-2}), the direct solar aerosol radiative effect is -1 W m^{-2} . The aerosol effectively enhances the reflectance above the ocean surface, but a distinct influence on the reflectance above savanna or grassland cannot be found. In agreement, Zhou *et al.* [2005]

found solar aerosol radiative effects of dust from -17 to -44 W m^{-2} per unit AOT at the TOA and -48 to -80 W m^{-2} per unit AOT at the surface from the Saharan desert (surface albedo ≈ 0.35) to the surrounding oceans (surface albedo ≈ 0.05). The change in surface albedo can even lead to a change of the radiative effect at the TOA from a general cooling effect to a heating effect [Bierwirth *et al.*, 2009; Tegen *et al.*, 2010].

5. Conclusion and Outlook

[31] In the framework of this study, vertical profiles of particle extinction were obtained with a shipborne Raman lidar aboard the German research vessel *Polarstern* during three meridional trans-Atlantic cruises [Kanitz *et al.*, 2013] and used as input for radiative transfer calculations. In the case of a lofted mixed layer with Saharan dust and biomass-burning smoke, a daily solar aerosol radiative effects of -15 W m^{-2} at TOA and -33 W m^{-2} at the surface were determined. The simulation of the incident irradiance was in good agreement to coincident pyranometer measurements.

[32] The complete lidar data set served for the first latitude-dependent investigation of the solar aerosol radiative effect of free-tropospheric and boundary-layer aerosol based on lidar-derived aerosol profile data. According to the determined frequent occurrence of free-tropospheric aerosol layers during the three meridional trans-Atlantic cruises, the direct solar aerosol radiative effect was highest in the latitudinal belt of the northern tropics from 15°N to the equator with -43 W m^{-2} at the surface and -14 W m^{-2} at TOA in the considered time periods. The radiative effect of the marine boundary layer alone showed low mean values of -3 to -7 W m^{-2} at the surface and -3 to -6 W m^{-2} at the TOA in all obtained latitudinal belts. The entire simulation results were compared to irradiance measurements at the surface. The best agreement for all simulations was found for cloud-free conditions at the surface. However, the uncertainties in the single scattering albedo and the phase function of the atmospheric aerosol particles remain as significant error sources in radiative transfer simulations.

[33] **Acknowledgments.** The funding by the Wilhelm Gottfried Leibniz Association (OCEANET project in the framework of PAKT) is appreciated. We thank the RV *Polarstern* team, the Alfred Wegener Institute for Polar and Marine Research (AWI), and the project leader of OCEANET Andreas Macke for their permanent support and interest in this work during the cruises ANT-XXVI and ANT-XXVII.

References

- Althausen, D., R. Engelmann, H. Baars, B. Heese, A. Ansmann, D. Müller, and M. Komppula (2009), Portable Raman lidar Polly^{XT} for automated profiling of aerosol backscatter, extinction, and depolarization, *J. Atmos. Oceanic Technol.*, *26*, 2366–2378, doi:10.1175/2009JTECHA1304.1.
- Anderson, G. P., S. A. Clough, F. X. Kneizys, J. H. Chetwynd, and E. P. Shettle (1986), AFGL atmospheric constituent profiles (0.120km).
- Ångström, A. (1929), On the atmospheric transmission of Sun radiation and on dust in the air, *Geogr. Ann.*, *11*, 156–166.
- Ansmann, A., M. Riebesell, and C. Weitkamp (1990), Measurement of atmospheric aerosol extinction profiles with a Raman lidar, *Opt. Lett.*, *15*, 746–748, doi:10.1364/OL.15.000746.
- Ansmann, A., U. Wandinger, M. Riebesell, C. Weitkamp, and W. Michaelis (1992), Independent measurement of extinction and backscatter profiles in cirrus clouds by using a combined Raman elastic-backscatter lidar, *Appl. Opt.*, *31*, 7113–7131, doi:10.1364/AO.31.007113.

- Ansmann, A., D. Althausen, U. Wandinger, K. Franke, D. Müller, F. Wagner, and J. Heintzenberg (2000), Vertical profiling of the Indian aerosol plume with six-wavelength lidar during INDOEX: A first case study, *Geophys. Res. Lett.*, *27*, 963–966, doi:10.1029/1999GL010902.
- Ansmann, A., F. Wagner, D. Müller, D. Althausen, A. Herber, W. von Hoyningen-Huene, and U. Wandinger (2002), European pollution outbreaks during ACE 2: Optical particle properties inferred from multiwavelength lidar and star-Sun photometry, *J. Geophys. Res.*, *107* (D15), 4259, doi:10.1029/2001JD001109.
- Bauer, S., E. Bierwirth, M. Esselborn, A. Petzold, A. Macke, T. Trautmann, and M. Wendisch (2011), Airborne spectral radiation measurements to derive solar radiative forcing of Saharan dust mixed with biomass burning smoke particles, *Tellus Ser. B*, *63*, 742–750, doi:10.1111/j.1600-0889.2011.00567.x.
- Bellouin, N., O. Boucher, M. Vesperini, and D. E. Tanré (2004), Estimating the direct aerosol radiative perturbation: Impact of ocean surface representation and aerosol non-sphericity, *Q. J. R. Meteorolog. Soc.*, *130*, 2217–2232, doi:10.1256/qj.03.136.
- Bierwirth, E., et al. (2009), Spectral surface albedo over Morocco and its impact on radiative forcing of Saharan dust, *Tellus Ser. B*, *61*, 252–269, doi:10.1111/j.1600-0889.2008.00395.x.
- Blanco-Muriel, M., D. C. Alarcón-Padilla, T. Lpez-Moratalla, and M. Lara-Coira (2001), Computing the solar vector, *Sol. Energy*, *70*(5), 431–441, doi:10.1016/S0038-092X(00)00156-0.
- Boucher, O., et al. (1998), Intercomparison of models representing direct shortwave radiative forcing by sulfate aerosols, *J. Geophys. Res.*, *103*(D14), 16,979–16,998, doi:10.1029/98JD00997.
- Bond, T. C., and R. W. Bergstrom (2006), Light absorption by carbonaceous particles: An investigative review, *Aerosol Sci. Technol.*, *40*, 27–67, doi:10.1080/02786820500421521.
- Christopher, S. A., and J. Zhang (2002), Shortwave aerosol radiative forcing from MODIS and CERES observations over the oceans, *Geophys. Res. Lett.*, *29*(18), 1859, doi:10.1029/2002GL014803.
- Cox, C., and W. Munk (1954a), Measurement of the roughness of the sea surface from photographs of the Sun's glitter, *J. Opt. Soc. Am.*, *44*, 838–850, doi:10.1364/JOSA.44.000838.
- Cox, C., and W. Munk (1954b), Statistics of the sea surface derived from Sun glitter, *J. Mar. Res.*, *13*, 198–227.
- Dentener, F., et al. (2006), Emissions of primary aerosol and precursor gases in the years 2000 and 1750, prescribed data-sets for AeroCom, *Atmos. Chem. Phys.*, *6*, 4321–4344, doi:10.5194/acp-6-4321-2006.
- Dirksen, R. J., K. Folkert Boersma, J. de Laat, P. Stammes, G. R. van der Werf, M. Val Martin, and H. M. Kelder (2009), An aerosol boomerang: Rapid around-the-world transport of smoke from the December 2006 Australian forest fires observed from space, *J. Geophys. Res.*, *114*, D21201, doi:10.1029/2009JD012360.
- Dubovik, O., B. Holben, T. F. Eck, A. Smirnov, Y. J. Kaufman, M. D. King, D. Tanré, and I. Slutsker (2002), Variability of absorption and optical properties of key aerosol types observed in worldwide locations, *J. Atmos. Sci.*, *59*, 590–608, doi:10.1175/1520-0469(2002)059<0590:VOAOP>2.0.CO;2.
- Duffot, V., P. Royer, P. Chazette, J. L. Baray, Y. Courcoux, and R. Delmas (2011), Marine and biomass burning aerosols in the southern Indian Ocean: Retrieval of aerosol optical properties from shipborne lidar and Sun photometer measurements, *J. Geophys. Res.*, *116*, D18208, doi:10.1029/2011JD015839.
- Fiebig, M., and J. A. Ogren (2006), Retrieval and climatology of the aerosol asymmetry parameter in the NOAA aerosol monitoring network, *J. Geophys. Res.*, *111*, D21204, doi:10.1029/2005JD006545.
- Forster, P., et al. (2007), *Climate Change 2007: The Physical Science basis. Contribution of Working Group I to the Fourth Assessment Report of the Intergovernmental Panel on Climate Change*, pp. 129–234, Chap. Changes in atmospheric constituents and in radiative forcing, Cambridge Univ. Press, Cambridge, U. K., and New York, 978 0 521 70596 7.
- Freudenthaler, V., et al. (2009), Depolarization ratio profiling at several wavelengths in pure Saharan dust during SAMUM 2006, *Tellus Ser. B*, *61*, 165–179, doi:10.1111/j.1600-0889.2008.00396.x.
- Groß, S., et al. (2011a), Characterization of the planetary boundary layer during SAMUM-2 by means of lidar measurements, *Tellus Ser. B*, *63*, 695–705, doi:10.1111/j.1600-0889.2011.00557.x.
- Groß, S., M. Tesche, V. Freudenthaler, C. Toledano, M. Wiegner, A. Ansmann, D. Althausen, and M. Seefeldner (2011b), Characterization of Saharan dust, marine aerosols and mixtures of biomass-burning aerosols and dust by means of multi-wavelength depolarization and Raman lidar measurements during SAMUM-2, *Tellus Ser. B*, *63*, 706–724, doi:10.1111/j.1600-0889.2011.00556.x.
- Haywood, J. M., and K. P. Shine (1997), Multi-spectral calculations of the direct radiative forcing of tropospheric sulphate and soot aerosols using a column model, *Q. J. R. Meteorolog. Soc.*, *123*, 1907–1930, doi:10.1002/qj.49712354307.
- Haywood, J. M., V. Ramaswamy, and B. J. Soden (1999), Tropospheric aerosol climate forcing in clear-sky satellite observations over the oceans, *Science*, *283*, 1299–1303, doi:10.1126/science.283.5406.1299.
- Heinold, B., I. Tegen, S. Bauer, and M. Wendisch (2011), Regional modelling of Saharan dust and biomass-burning smoke. Part 2: Direct radiative forcing and atmospheric dynamic response, *Tellus Ser. B*, *63*, 800–813, doi:10.1111/j.1600-0889.2011.00574.x.
- Huang, J., Q. Fu, J. Su, Q. Tang, P. Minnis, Y. Hu, Y. Yi, and Q. Zhao (2009), Taklimakan dust aerosol radiative heating derived from CALIPSO observations using the Fu-Liou radiation model with CERES constraints, *Atmos. Chem. Phys.*, *9*(12), 4011–4021, doi:10.5194/acp-9-4011-2009.
- Johnson, B. T., B. Heese, S. A. McFarlane, P. Chazette, A. Jones, and N. Bellouin (2008), Vertical distribution and radiative effects of mineral dust and biomass burning aerosol over West Africa during DABEX, *J. Geophys. Res.*, *113*, D00C12, doi:10.1029/2008JD009848.
- Kalisch, J., and A. Macke (2008), Estimation of the total cloud cover with high temporal resolution and parametrization of short-term fluctuations of sea surface insolation, *Meteorol. Z.*, *17*, 603–611.
- Kalisch, J., and A. Macke (2012), Radiative budget and cloud radiative effect over the Atlantic from ship-based observations, *Atmos. Meas. Tech.*, *5*(10), 2391–2401, doi:10.5194/amt-5-2391-2012.
- Kanamitsu, M. (1989), Description of the NMC global data assimilation and forecast system, *Weather Forecast.*, *4*, 335–342, doi:10.1175/1520-0434(1989)004<0335:DOTNGD>2.0.CO;2.
- Kanitz, T., P. Seifert, A. Ansmann, R. Engelmann, D. Althausen, C. Casaccia, and E. G. Rohwer (2011), Contrasting the impact of aerosols at northern and southern midlatitudes on heterogeneous ice formation, *Geophys. Res. Lett.*, *38*, L17802, doi:10.1029/2011GL048532.
- Kanitz, T., A. Ansmann, R. Engelmann, and D. Althausen (2013), North-south cross sections of aerosol layering over the Atlantic Ocean from multiwavelength Raman/polarization lidar during Polarstern cruises, *J. Geophys. Res. Atmospheres*, *118*, 2643–2655, doi:10.1002/jgrd.50273.
- Kato, S., T. P. Ackerman, J. H. Mather, and E. E. Clothiaux (1999), The k-distribution method and correlated-k approximation for a short-wave radiative transfer model, *J. Quant. Spectrosc. Radiat. Transfer*, *62*, 109–121, doi:10.1016/S0022-4073(98)00075-2.
- Kaufman, Y., I. Koren, L. Remer, D. Rosenfeld, and Y. Rudich (2005), The effect of smoke, dust, and pollution aerosol on shallow cloud development over the Atlantic Ocean, *Proc. Nat. Acad. Sci. U. S. A.*, *102*, 11,207–11,212, doi:10.1073/pnas.0505191102.
- Keil, A., and J. M. Haywood (2003), Solar radiative forcing by biomass burning aerosol particles during SAFARI 2000: A case study based on measured aerosol and cloud properties, *J. Geophys. Res.*, *108*(D13), 8467, doi:10.1029/2002JD002315.
- Kim, D., M. Chin, H. Yu, T. F. Eck, A. Sinyuk, A. Smirnov, and B. N. Holben (2011), Dust optical properties over North Africa and Arabian Peninsula derived from the AERONET dataset, *Atmos. Chem. Phys.*, *11*, 10,733–10,741, doi:10.5194/acp-11-10733-2011.
- Kipp and Zonen (2004), *Instruction Manual CM21—Manual Version: 0904*, Kipp & Zonen B.V., Delftechpark 36, 2628 Delft, Nederlande.
- Klett, J. D. (1981), Stable analytical inversion solution for processing lidar returns, *Appl. Opt.*, *20*, 211–220, doi:10.1364/AO.20.000211.
- Koffi, B., et al. (2012), Application of the CALIOP layer product to evaluate the vertical distribution of aerosols estimated by global models: AeroCom phase I results, *J. Geophys. Res.*, *117*, D10201, doi:10.1029/2011JD016858.
- Kylling, A. (1992), Radiation transport in cloudy and aerosol loaded atmospheres, Ph. D. thesis, Alaska University, Fairbanks.
- Liao, H., and J. H. Seinfeld (1998), Radiative forcing by mineral dust aerosols: Sensitivity to key variables, *J. Geophys. Res.*, *103*, 31,637–31,646, doi:10.1029/1998JD200036.
- Macke, A., J. Kalisch, Y. Zöll, and K. Bumke (2010), Radiative effects of the cloudy atmosphere from ground and satellite based observations, *EPJ Web Conf.*, *9*, 83–94, doi:10.1051/epjconf/201.009006.
- Mallet, M., et al. (2008), Aerosol direct radiative forcing over Djougou (northern Benin) during the African Monsoon Multidisciplinary Analysis dry season experiment (special observation period-0), *J. Geophys. Res.*, *113*, D00C01, doi:10.1029/2007JD009419.
- Mattis, I., A. Ansmann, D. Müller, U. Wandinger, and D. Althausen (2004), Multiyear aerosol observations with dual-wavelength raman lidar in the framework of EARLINET, *J. Geophys. Res.*, *109*, D13203, doi:10.1029/2004JD004600.
- Mattis, I., D. Müller, A. Ansmann, U. Wandinger, J. Preißler, P. Seifert, and M. Tesche (2008), Ten years of multiwavelength Raman lidar observations of free-tropospheric aerosol layers over central Europe: Geometrical properties and annual cycle, *J. Geophys. Res.*, *113*, D20202, doi:10.1029/2007JD009636.
- Mayer, B., and A. Kylling (2005), Technical note: The libRadtran software package for radiative transfer calculations—description and examples of use, *Atmos. Chem. Phys.*, *5*, 1855–1877, doi:10.5194/acp-5-1855-2005.

- Meloni, D., A. di Sarra, G. Pace, and F. Monteleone (2006), Aerosol optical properties at Lampedusa (central Mediterranean). 2. Determination of single scattering albedo at two wavelengths for different aerosol types, *Atmos. Chem. Phys.*, *6*, 715–727, doi:10.5194/acp-6-715-2006.
- Mishchenko, M. I., L. D. Travis, R. A. Kahn, and R. A. West (1997), Modeling phase functions for dustlike tropospheric aerosols using a shape mixture of randomly oriented polydisperse spheroids, *J. Geophys. Res.*, *102*, 16,831–16,847, doi:10.1029/96JD02110.
- Müller, D., U. Wandinger, and A. Ansmann (1999), Microphysical particle parameters from extinction and backscatter lidar data by inversion with regularization: Theory, *Appl. Opt.*, *38*, 2346–2357, doi:10.1364/AO.38.002346.
- Müller, D., A. Ansmann, I. Mattis, M. Tesche, U. Wandinger, D. Althausen, and G. Pisani (2007), Aerosol-type-dependent lidar ratios observed with Raman lidar, *J. Geophys. Res.*, *112*, D16202, doi:10.1029/2006JD008292.
- Müller, T., A. Schladitz, K. Kandler, and A. Wiedensohler (2011), Spectral particle absorption coefficients, single scattering albedos and imaginary parts of refractive indices from ground based in situ measurements at Cape Verde Island during SAMUM-2, *Tellus Ser. B*, *63*, 573–588, doi:10.1111/j.1600-0889.2011.00572.x.
- Osborne, S. R., A. J. Baran, B. T. Johnson, J. M. Haywood, E. Hesse, and S. Newman (2011), Short-wave and long-wave radiative properties of Saharan dust aerosol, *Q. J. R. Meteorol. Soc.*, *137*, 1149–1167, doi:10.1002/qj.771.
- Otto, S., E. Bierwirth, B. Weinzierl, K. Kandler, M. Esselborn, M. Tesche, A. Schladitz, M. Wendisch, and T. Trautmann (2009), Solar radiative effects of a Saharan dust plume observed during SAMUM assuming spheroidal model particles, *Tellus Ser. B*, *61*, 270–296, doi:10.1111/j.1600-0889.2008.00389.x.
- Petzold, A., A. Veira, S. Mund, M. Esselborn, C. Kiemle, B. Weinzierl, T. Hamburger, G. Ehret, K. Liebke, and K. Kandler (2011), Mixing of mineral dust with urban pollution aerosol over Dakar (Senegal): Impact on dust physico-chemical and radiative properties, *Tellus Ser. B*, *63*, 619–634, doi:10.1111/j.1600-0889.2011.00547.x.
- Podgorny, I. A., and V. Ramanathan (2001), A modeling study of the direct effect of aerosols over the tropical Indian Ocean, *J. Geophys. Res.*, *106*, 24,097–24,106, doi:10.1029/2001JD900214.
- Preißler, J., F. Wagner, J. L. Guerrero-Rascado, and A. M. Ansmann (2013), Two years of free-tropospheric aerosol layers observed over Portugal by lidar, *J. Geophys. Res. Atmospheres*, *118*, 3676–3686, doi:10.1002/jgrd.50350.
- Ramanathan, V., R. D. Cess, E. F. Harrison, P. Minnis, B. R. Barkstrom, E. Ahmad, and D. Hartmann (1989), Cloud-radiative forcing and climate: Results from the Earth radiation budget experiment, *Science*, *243*, 57–63, doi:10.1126/science.243.4887.57.
- Redemann, J., R. P. Turco, K. N. Liou, P. V. Hobbs, W. S. Hartley, R. W. Bergstrom, E. V. Browell, and P. B. Russell (2000), Case studies of the vertical structure of the direct shortwave aerosol radiative forcing during TARFOX, *J. Geophys. Res.*, *105*, 9971–9980, doi:10.1029/1999JD901042.
- Reid, J. S., P. V. Hobbs, R. J. Ferek, D. R. Blake, J. V. Martins, M. R. Dunlap, and C. Liou (1998), Physical, chemical, and optical properties of regional hazes dominated by smoke in Brazil, *J. Geophys. Res.*, *103*, 32,059–32,080, doi:10.1029/98JD00458.
- Reid, J. S., E. M. Prins, D. L. Westphal, C. C. Schmidt, K. A. Richardson, S. A. Christopher, T. F. Eck, E. A. Reid, C. A. Curtis, and J. P. Hoffman (2004), Real-time monitoring of South American smoke particle emissions and transport using a coupled remote sensing/box-model approach, *Geophys. Res. Lett.*, *31*, L06107, doi:10.1029/2003GL018845.
- Reid, J. S., T. F. Eck, S. A. Christopher, R. Koppmann, O. Dubovik, D. P. Eleuterio, B. N. Holben, E. A. Reid, and J. Zhang (2005), A review of biomass burning emissions part III: Intensive optical properties of biomass burning particles, *Atmos. Chem. Phys.*, *5*, 827–849, doi:10.5194/acp-5-827-2005.
- Roger, J. C., M. Mallet, P. Dubuisson, H. Cachier, E. Vermote, O. Dubovik, and S. Despiou (2006), A synergetic approach for estimating the local direct aerosol forcing: Application to an urban zone during the Experience sur Site pour Contraindre les Modeles de Pollution et de Transport d'Emission (ESCOMPTE) experiment, *J. Geophys. Res.*, *111*, D13208, doi:10.1029/2005JD006361.
- Sasano, Y., E. V. Browell, and S. Ismail (1985), Error caused by using a constant extinction/backscattering ratio in the lidar solution, *Appl. Opt.*, *24*, 3929–3932, doi:10.1364/AO.24.003929.
- Singh, H. B., et al. (2000), Biomass burning influences on the composition of the remote South Pacific troposphere: Analysis based on observations from PEM-Tropics-A, *Atmos. Environ.*, *34*, 635–644, doi:10.1016/S1352-2310(99)00380-5.
- Schade, N. H., A. Macke, H. Sandmann, and C. Stick (2007), Enhanced solar global irradiance during cloudy sky conditions, *Meteorol. Z.*, *16*(3), 295–303.
- Shettle, E. P. (1979), Models for the aerosols of the lower atmosphere and the effects of humidity variations on their optical properties, *Tech. Rep.*, DTIC Document.
- Smirnov, A., et al. (2009), Maritime aerosol network as a component of aerosol robotic network, *J. Geophys. Res.*, *114*, D06204, doi:10.1029/2008JD011257.
- Sokolik, I. N., and O. B. Toon (1999), Incorporation of mineralogical composition into models of the radiative properties of mineral aerosol from UV to IR wavelengths, *J. Geophys. Res.*, *104*, 9423–9444, doi:10.1029/1998JD200048.
- Sokolik, I. N., D. M. Winker, G. Bergametti, D. A. Gillette, G. Carmichael, Y. J. Kaufman, L. Gomes, L. Schuetz, and J. E. Penner (2001), Introduction to special section: Outstanding problems in quantifying the radiative impacts of mineral dust, *J. Geophys. Res.*, *106*, 18,015–18,028, doi:10.1029/2000JD900498.
- Stamnes, K., S.-C. Tsay, K. Jayaweera, and W. Wiscombe (1988), Numerically stable algorithm for discrete-ordinate-method radiative transfer in multiple scattering and emitting layered media, *Atmos. Opt.*, *27*, 2502–2509, doi:10.1364/AO.27.002502.
- Takemura, T., T. Nakajima, O. Dubovik, B. N. Holben, and S. Kinne (2002), Single-scattering albedo and radiative forcing of various aerosol species with a global three-dimensional model, *J. Clim.*, *15*, 333–352, doi:10.1175/1520-0442(2002)015<0333:SSAARF>2.0.CO;2.
- Tegen, I., and A. A. Lacis (1996), Modeling of particle size distribution and its influence on the radiative properties of mineral dust aerosol, *J. Geophys. Res.*, *101*, 19,237–19,244, doi:10.1029/95JD03610.
- Tegen, I., E. Bierwirth, B. Heinold, J. Helmert, and M. Wendisch (2010), Effect of measured surface albedo on modeled Saharan dust solar radiative forcing, *J. Geophys. Res.*, *115*, D24312, doi:10.1029/2009JD013764.
- Tesche, M., A. Ansmann, D. Müller, D. Althausen, R. Engelmann, V. Freudenthaler, and S. Groß (2009), Vertically resolved separation of dust and smoke over Cape Verde using multiwavelength Raman and polarization lidars during Saharan Mineral Dust Experiment 2008, *J. Geophys. Res.*, *114*, D13202, doi:10.1029/2009JD011862.
- Tesche, M., S. Gross, A. Ansmann, D. Müller, D. Althausen, V. Freudenthaler, and M. Esselborn (2011), Profiling of Saharan dust and biomass-burning smoke with multiwavelength polarization Raman lidar at Cape Verde, *Tellus Ser. B*, *63*, 649–676, doi:10.1111/j.1600-0889.2011.00548.x.
- Textor, C., et al. (2006), Analysis and quantification of the diversities of aerosol life cycles within AeroCom, *Atmos. Chem. Phys.*, *6*, 1777–1813, doi:10.5194/acp-6-1777-2006.
- Trenberth, K. E., J. T. Fasullo, and J. Kiehl (2009), Earth's global energy budget, *Bull. Am. Meteorol. Soc.*, *90*, 311–323, doi:10.1175/2008BAMS2634.1.
- Wagner, F., D. Müller, and A. Ansmann (2001), Comparison of the radiative impact of aerosols derived from vertically resolved (lidar) and vertically integrated (Sun photometer) measurements: Example of an Indian aerosol plume, *J. Geophys. Res.*, *106*, 22,861–22,870, doi:10.1029/2001JD000320.
- Wandinger, U., and A. Ansmann (2002), Experimental determination of the lidar overlap profile with Raman lidar, *Appl. Opt.*, *41*, 511–514, doi:10.1364/AO.41.000511.
- Wendisch, M., S. Mertes, A. Ruggaber, and T. Nakajima (1996), Vertical profiles of aerosol and radiation and the influence of a temperature inversion: Measurements and radiative transfer calculations, *J. Appl. Meteorol.*, *35*, 1703–1715, doi:10.1175/1520-0450(1996)035<1703:VPOAAR>2.0.CO;2.
- Wendisch, M., D. Müller, I. Mattis, and A. Ansmann (2006), Potential of lidar backscatter data to estimate solar aerosol radiative forcing, *Appl. Opt.*, *45*(4), 770–783, doi:10.1364/AO.45.000770.
- Wielicki, B. A., B. R. Barkstrom, E. F. Harrison, R. B. Lee, G. L. Smith, and J. E. Cooper (1996), Clouds and the Earth's radiant energy system (CERES): An Earth Observing System Experiment, *Bull. Am. Meteorol. Soc.*, *77*, 853–868, doi:10.1175/1520-0477(1996)077<0853:CATERE>2.0.CO;2.
- Winker, D. M., M. A. Vaughan, A. Omar, Y. Hu, K. A. Powell, Z. Liu, W. H. Hunt, and S. A. Young (2009), Overview of the CALIPSO mission and CALIOP data processing algorithms, *J. Atmos. Oceanic Technol.*, *26*, 2310–2323, doi:10.1175/2009JTECHA1281.1.
- Yu, H., M. Chin, D. M. Winker, A. H. Omar, Z. Liu, C. Kittaka, and T. Diehl (2010), Global view of aerosol vertical distributions from CALIPSO lidar measurements and GOCART simulations: Regional and seasonal variations, *J. Geophys. Res.*, *115*, D00H30, doi:10.1029/2009JD013364.
- Zhou, M., H. Yu, R. E. Dickinson, O. Dubovik, and B. N. Holben (2005), A normalized description of the direct effect of key aerosol types on solar radiation as estimated from aerosol robotic network aerosols and moderate resolution imaging spectroradiometer albedos, *J. Geophys. Res.*, *110*, D19202, doi:10.1029/2005JD005909.